Effects of Coronal and Shock-Produced X-Rays on the Ionization Distribution in Hot Star Winds

J.J. MacFarlane, W.L. Waldron, M.F. Corcoran,
M.J. Wolff, P. Wang, J.P. Cassinelli

March 1993

UWFDM-912

Astrophysical Journal (1993).

FUSION TECHNOLOGY INSTITUTE

UNIVERSITY OF WISCONSIN

MADISON WISCONSIN

EFFECTS OF CORONAL AND SHOCK-PRODUCED X-RAYS ON THE IONIZATION DISTRIBUTION IN HOT STAR WINDS

J.J. MacFarlane
Department of Astronomy and Fusion Technology Institute
University of Wisconsin
Madison, WI 53706

W.L. Waldron
Applied Research Corporation
8201 Corporate Drive, Suite 920
Landover, MD 20785

M.F. Corcoran
Universities Space Research Association
Goddard Space Flight Center
Greenbelt, MD 20771

M.J. Wolff
Department of Astronomy
University of Wisconsin
Madison, WI 53706

P. Wang
Fusion Technology Institute
University of Wisconsin
Madison, WI 53706

and

J.P. Cassinelli
Department of Astronomy
University of Wisconsin
Madison, WI 53706

March 1993

UWFDM-912

Submitted to Astrophysical Journal

Abstract

We investigate the effects of X-ray radiation on the ionization distribution in the wind of ζ Pup (O4 If). In particular we have studied how the distribution of the "superionization" species OVI is affected by X-ray source characteristics. In our calculations, detailed statistical equilibrium and atomic physics models are used to ensure that critical processes such as photoionization out of excited states and Auger ionization are considered. For shock-produced X-ray sources we show how the distribution of X-ray emission affects the OVI P-Cygni profile and the resultant X-ray spectrum. For coronal sources we examine the sensitivity of the X-ray spectrum and OVI profile to the mass loss rate and attenuation by the overlying wind. Results are compared with UV data from *Copernicus* and X-ray spectral data from the *Einstein* IPC and BBXRT. We find that coronal models are consistent with both UV and X-ray data but only if the mass loss rate is $\lesssim 1 \times 10^{-6}$ $M_\odot$/yr, which is a factor of at least 3 to 5 lower than the values deduced from radio observations. Results from calculations using a mass loss rate inferred from radio observations suggest that the X-ray source is distributed throughout the wind. In addition, calculations using a distributed X-ray source indicate that a significant X-ray flux must originate from regions close to the star (within 2 stellar radii) in order to produce an OVI P-Cygni profile consistent with observations.

I. Introduction

Since X-ray emission from early-type stars was discovered more than a decade ago (Harnden et al. 1979; Seward et al. 1979; Long and White 1980; Cassinelli et al. 1981) the source of the X-rays has been the subject of debate. Observations indicate that O stars have X-ray luminosities of $L_{\rm X} \sim 10^{-7}\, L_{bol}$ (Sciortino et al. 1990) with characteristic plasma temperatures of $10^6 - 10^7$ K (Chlebowski et al. 1989). The observed presence of "superionization" states OVI and NV in the winds of hot stars led Cassinelli and Olson (1979) to propose that X-rays from a thin base corona produce the ions by way of the Auger effect. Olson (1978) and Olson and Castor (1981) used the base coronal model to interpret the UV resonance line profiles of these ions. Observations from the Imaging Proportional Counter (IPC) (Long and White 1980; Cassinelli et al. 1981) and the Solid State Spectrometer (SSS) (Cassinelli and Swank 1983) failed to show evidence of K-shell photoabsorption from oxygen present in the overlying cool wind. Coronal model calculations using mass loss rates inferred from radio observations indicate that such K-shell attenuation should have been observable. This suggested that at least part of the X-rays originate above the base of the cool wind. Recent observations of ζ Pup using the Broad-Band X-ray Telescope (BBXRT) (Corcoran et al. 1992) have provided the first detection of oxygen K-shell photoabsorption due to the overlying wind. However, using a mass loss rate based on radio data, the measured optical depth was found to be consistent with an X-ray source located significantly above the photosphere, but at less than 10 stellar radii.

Waldron (1984) argued that if the coronal luminosity is sufficiently high and its effect on the overlying wind is taken into account, the coronal hypothesis cannot be ruled out. Baade and Lucy (1987) argued that the lack of detection of the Fe XIV 5303 Å coronal emission line, which would be expected to be observable if coronal parameters predicted by Waldron (1984) and Cassinelli et al. (1981) are correct, strongly suggests that the bulk of the X-rays are embedded in the wind. It is important to note, however, that the 5303 Å line is only be expected to be observed for coronal plasma temperatures $\lesssim 4 \times 10^6$ K and emission measures $\gtrsim 10^{57}$ cm^{-3}.

An alternative explanation for the origin of X-rays is that strong shocks form in the winds of hot stars due to radiatively-driven instabilities (Lucy and White 1980; Lucy 1982). In this scenario K-shell attenuation by oxygen need not be as significant because the column density of the overlying cool plasma between the shock and the observer is reduced. Owocki and Rybicki (1984, 1986), Owocki et al. (1988), and Owocki (1991)

performed detailed analyses of the formation and growth of shocks due to line driven instabilities. Calculations using a pure absorption model (Owocki et al. 1988) predict that instabilities evolve very rapidly (starting within $r \lesssim 1.5\,R_*$) into strong shocks. More recent calculations which include scattering effects (Owocki 1991) indicate that while scattering can significantly damp the growth of the instability, strong shocks can still be generated. In other studies, Mullen (1984) proposed that corotating interaction regions, in which shocks evolve to a "spiral-type" structure as faster components of the wind overtake slower components, could readily explain both the X-rays and the observed presence of narrow absorption features in UV P-Cygni profiles (Lamers et al. 1982). MacFarlane and Cassinelli (1989) showed that even the observed X-ray emission from stars with relatively low mass loss rates (e.g., τ Sco, B0 V) could also be explained by wind shocks.

Additional hypotheses for the origin of X-rays from early type stars have also been recently proposed. Chen and White (1991) argued that relatively hard X-rays with photon energies $\gtrsim 2$ keV could be produced as UV photons are scattered by relativistic electrons which are accelerated in wind shocks. Cheblowski (1989) has suggested that the X-rays are not related to wind conditions near the star, but instead are produced from the interaction of the stellar wind with circumstellar matter.

It is widely believed that the X-ray radiation field is responsible for the observed presence of OVI in the winds of many early-type stars for the following reasons: (1) the observed X-ray flux is sufficient to produce quantities of OVI consistent with UV observations (Olson and Castor 1981); and (2) OVI has been observed for stars as late as B0 - B1 (Cassinelli and Olson 1979), whereas ionization equilibrium calculations (Drew 1989) indicate that very little OVI should be present in the winds of late O and early B stars. Interestingly, Pauldrach (1987) argued that OVI can be produced in the winds of hot stars without X-rays. However, this seems unlikely to be true for late-O and early-B stars because of their lower effective temperatures. Furthermore, Pauldrach neglected to include in his calculations the process of dielectronic recombination, a process which has been shown to be extremely important — quite often the dominant recombination process — even at relatively cool plasma temperatures ($T \sim 10^4 - 10^5$ K; Nussbaumer and Storey 1983, 1984).

If indeed OVI is produced by the X-ray radiation field, then it seems that additional information concerning the X-ray source location might be obtained from its UV P-Cygni profile. One of the primary objectives of this paper is to show how the

OVI P-Cygni profile, in conjunction with X-ray spectral data, can be used to further constrain the characteristics of the X-ray source. In particular, we examine under what conditions these two types of observational data are compatible with the various X-ray source hypotheses. To do this we have performed a series of ionization balance calculations for a particularly well-studied star: ζ Pup (O4 If). The X-ray distribution in our calculations is modeled in one of 2 ways: (1) a thin corona at the base of the wind; or (2) a distributed X-ray source meant to resemble a series of many shocks propagating through the wind. In addition, fairly elaborate atomic models are used so that both Auger ionization from the X-rays and photoionization out of excited states could be properly taken into account. The latter process has been shown to be crucial in determining the ionization properties of hot star winds (Pauldrach 1987; Drew 1989). But while the previous studies of Drew and Pauldrach made notable advances in our understanding of the ionization structure of hot star winds, neither considered the effects of the X-ray radiation field on the ionization balance.

In this paper, we describe results from ionization balance calculations for ζ Pup which show the dependence of the OVI distribution and the resulting P-Cygni profile on the location of the X-ray source. We have used the UV P-Cygni profile observed by Copernicus (Morton 1976) and X-ray spectra obtained from the Einstein IPC (Cassinelli et al. 1981) and BBXRT (Corcoran et al. 1992) as observational constraints. For coronal models, we set limits for wind and X-ray parameters which are consistent with both the X-ray and UV data. For shock models we attempt to deduce the region (radius) where a significant fraction of the X-rays start to form. In addition, we examine which processes are most responsible for producing the OVI, and describe the sensitivity of the OVI profiles to some of the uncertainties in the calculations, such as the temperature distribution in the wind.

II. Model Description

(a) Wind Parameters

We assume a spherically symmetric expanding wind with a wind particle (ion) density given by:

$$n_w(r) = \frac{\dot{M}}{4\pi r^2 v(r) \mu \mathrm{m_H}}\,, \tag{1}$$

where $\dot{M}$ is the mass loss rate and μm_H is the average atomic mass for the wind. The velocity field at radius r is specified by

$$v(r) = v_0 + (v_\infty - v_0)\left(1 - \frac{R_*}{r}\right)^\beta , \tag{2}$$

where v_∞ is the terminal velocity, R_* is the radius of the star, and v_0 is the minimum velocity at the base of the wind. For ζ Pup, we take β to have a value of 0.7, $R_* = 16\,R_\odot$, $v_\infty = 2200$ km/sec (Groenewegen and Lamers 1989), and $v_0 = 0.01 v_\infty$.

The mass loss rate was adjusted between the range of 1×10^{-6} and 5×10^{-6} $M_\odot$/yr. By comparison, the values deduced from radio observations are 3.5×10^{-6} $M_\odot$/yr (Abbott et al. 1980) and 5×10^{-6} $M_\odot$/yr (Bieging et al. 1989), while that from UV observations is 7×10^{-6} $M_\odot$/yr (Lamers and Morton 1976). Determining mass loss rates from UV observations is very difficult due to uncertainties in the ionization distribution and the fact that the P-Cygni lines tend to be nearly saturated for ζ Pup (Groenewegen and Lamers 1989).

The wind temperature is potentially a major source of uncertainty in determining the ionization balance. Early work by Klein and Castor (1980) using H-He wind models predicted wind temperatures to be about 0.8 $T_{\rm eff}$. However, Drew (1989) has shown that cooling due to heavy element line radiation can result in significantly lower temperatures — as low as 0.3 $T_{\rm eff}$ at $r = 10\,R_*$. In our calculations for ζ Pup, we have chosen a temperature distribution from Drew's results as our base case. To assess the sensitivity of our results to uncertainties in the wind temperature, several calculations were also performed using $T = T_{\rm eff}$.

(b) Statistical Equilibrium

The distribution of atomic level populations throughout the wind is determined by solving multilevel statistical equilibrium equations. The steady-state rate equation for atomic level n can be written as (see e.g., Klein and Castor 1978):

$$\sum_{m<n} \left[n_m\left(B_{mn}\,\mathcal{J}_{mn} + n_e\,C_{mn}\right) - n_n\left(A_{nm} + B_{nm}\,\mathcal{J}_{mn} + n_e\,C_{nm}\right)\right]$$

$$+ \sum_{m>n} \left[n_m\left(A_{mn} + B_{mn}\mathcal{J}_{mn} + n_e\,C_{mn}\right) - n_n\left(B_{nm}\,\mathcal{J}_{mn} + n_e\,C_{nm}\right)\right]$$

$$+ n^*_{n,\kappa}\, n_e\, C_{n,\kappa} + \sum_\kappa\, n^*_{n,\kappa}\, \left[\int_{\nu_{n,\kappa}}^{\alpha}\, \frac{4\pi}{h\nu}\, \alpha_{n,\kappa}(\nu)\, \left(\frac{2h\nu^3}{c^2} + J_\nu\right)\, \exp\left(-\frac{h\nu}{kT}\right)\, d\nu\right]$$

$$- n_n\, n_e\, C_{n,\kappa} - \sum_\kappa\, n_n\, \left[\int_{\nu_{n,\kappa}}^{\alpha}\, \frac{4\pi}{h\nu}\, \alpha_{n,\kappa}(\nu) J_\nu\, d\nu\right] - n_\kappa\, n_e\, \alpha_{DR} = 0\,. \tag{3}$$

The first two summations include the collisional and radiative rates for all bound-bound transitions. The quantities n_e and n_m represent the electron density and number density of particles in atomic level m, respectively. The Einstein coefficients are given by A_{mn} and B_{mn}, while the collision rate coefficients are represented by C_{mn}. The mean intensity averaged over the line profile, $\mathcal{J}_{mn}$, is computed using the Sobolev approximation (Castor 1970):

$$\begin{aligned} \mathcal{J}_{mn} &= (1-\beta_{mn})\, \frac{2h\nu^3_{mn}}{c^2}\, \left[\frac{n_m}{n_n}\, \frac{g_n}{g_m} - 1\right]^{-1} \\ &+ \beta_{c,mn}\, I_c(\nu_{mn})\,, \end{aligned} \tag{4}$$

where $h\nu_{mn}$ is the energy of the line transition, g_m and g_n are the statistical weights, and $I_c\,(\nu_{mn})$ is the photospheric radiation intensity at the frequency of the transition. The quantities β_{mn} and $\beta_{c,mn}$ are angle-integrated escape probability functions given by

$$\beta_{mn} = \int_0^1\, \frac{1+\sigma x^2}{\tau_{mn}}\, \left[1 - \exp\left(-\frac{\tau_{mn}}{1+\sigma x^2}\right)\right]\, dx$$

and

$$\beta_{c,mn} = \frac{1}{2}\, \int_{x_1}^1\, \frac{1+\sigma x^2}{\tau_{mn}}\, \left[1 - \exp\left(-\frac{\tau_{mn}}{1+\sigma x^2}\right)\right]\, dx\,, \tag{5}$$

where

$$x_1 = (1 - R^2_*/r^2)^{1/2}$$

and σ is defined by the radial derivative of the wind velocity $v(r)$:

$$\sigma = \frac{d\, \ln\, v(r)}{d\, \ln\, r} - 1\,.$$

In Eq. (5), the optical depth τ_{mn} is given by

$$\tau_{mn} = \frac{\pi e^2}{m_e c}\, f_{mn}\, (n_m - \frac{g_m}{g_n}\, n_n)\, \lambda_{mn}\, \frac{r}{v(r)}\,,$$

where f_{mn} and λ_{mn} are the oscillator strength and wavelength for the transition.

The ionization and recombination processes included in Eq. (3) are as follows. The upper state of such transitions is represented by the index κ. The quantity $n^*_{n,\kappa}$ is the LTE value of n_n determined from the values of n_e, n_κ, and the temperature T (see, e.g., Mihalas 1978). Photoionization of electrons out of all subshells is computed. For K-shell photoionization, autoionization to the ground state of the next higher ionization stage is assumed (e.g., OIV goes directly to OVI). The cutoff frequency and photoionization cross section are given by $\nu_{n,\kappa}$ and $\alpha_{n,\kappa}(\nu)$, respectively. The calculation of the mean intensity, J_ν, is discussed below. The last term in Eq. (3) is the contribution from dielectronic recombination. This is often the dominant recombination process for many ions at the conditions prevalent in stellar winds. In our model, we consider dielectronic recombination between ground states of adjacent ions only. The rate coefficients (α_{DR}) are obtained by the formulae of Nussbaumer and Storey (1983).

(c) Atomic Models

Our model wind is composed of six elements — H, He, C, N, O, and Si — in proportions given by the cosmic abundances of Allen (1973). A total of 203 atomic levels and 26 ionization stages were considered. A disproportionately large number of levels (70) were considered for oxygen because of our particular interest in predicting the OVI distribution in the wind.

Energy levels, oscillator strengths, and photoionization cross sections were obtained from Hartree-Fock calculations. L-S coupling was used to model the angular momentum coupling between electrons. For each level, photoionization cross sections were computed for electrons in each subshell and fit to the formula

$$\sigma(\nu) = \sigma(\nu_1) \left\{ (1-\beta) \left(\frac{\nu_1}{\nu} \right)^s + \beta \left(\frac{\nu_1}{\nu} \right)^{s+1} \right\} , \tag{6}$$

where ν_1 is the cutoff frequency, and β and s are parameters obtained from the fitting procedure. Cross sections were computed for each subshell of all states so that all photoionization processes, including Auger ionization and photoionization out of and into excited states, could be treated.

Collisional rate coefficients for all electric dipole-allowed transitions were computed using a semi-classical impact parameter model (Burgess and Summer 1976). In addition, distorted wave (Sobelman et al. 1981) calculations were performed to obtain collisional

rate coefficients for forbidden transitions involving the ground state of each ion. Thus, all excited states were coupled with the ground state in our atomic models, while all allowed transitions between excited states were collisionally coupled. Although collisional ionization and recombination tend not to be important processes in the cool portion of hot star winds, collisional excitation can be an important process (Pauldrach 1987). A detailed description of the atomic physics models is given elsewhere (Wang 1991).

(d) Radiation Field

The radiation field includes contributions from 3 components: the photosphere, diffuse radiation from the wind, and X-ray radiation from a hot ($T > 10^6$ K) plasma. At photon energies below the He II Lyman continuum edge the radiation field is dominated by photospheric radiation. We assume the wind continuum opacity below this energy is negligible so that the mean intensity and the continuum specific intensity in Eq. (3) are given by:

$$J_\nu = 4\,W\,H_\nu\,,$$

and

$$I_{c,\nu} = 4\,H_\nu\,, \tag{7}$$

where W is the local dilution factor, and H_ν is the Eddington flux at the top of the photosphere as prescribed by Mihalas (1972). The entire wind is considered "external" to the photosphere and there is no influence from the wind on the photosphere ("core-halo" approximation). Since ζ Pup's photospheric parameters ($T_{\rm eff} = 42,000$ K, log g = 3.8) lie between the grid of non-LTE atmospheres models computed by Mihalas, the Eddington fluxes were obtained by logarithmic interpolation between the $T_{\rm eff} = 45{,}000$ K, log g = 4.0 and $T_{\rm eff} = 40{,}000$ K, log g = 3.5 models.

The diffuse radiation field is approximated by assuming that the mean intensity at each point is specified by the source function for the "dominant" bound-free transition. That is,

$$J_\nu = \frac{B_\nu\,(T(r))}{b_1(r)}\,, \tag{8}$$

where B_ν is the Planck function at the local wind temperature, and b_1 is the LTE departure coefficient for the transition. At photon energies between 54.4 and 77.4 eV, we use a departure coefficient for the He II ground state. Above 77.4 eV and 113.9, the OIV and OV ground state departure coefficients are used, respectively.

X-ray emission is modeled with an isothermal high temperature plasma region. The source is located either at the base of the wind (corona) or is distributed throughout the wind (shocks). The mean intensity at each frequency and each spatial point is obtained by solving the integral form of the radiative transfer equation along a grid of impact parameter rays. The X-ray emissivity can be expressed as:

$$\eta_\nu^{\rm x}(r) = \frac{1}{4\pi}\,\Gamma(r)\,\Lambda_\nu\,, \tag{9}$$

where $\Gamma(r)$ is the volume derivative of the X-ray emission measure, $EM_{\rm x}\,(\equiv \int\, d\,V\,n_e^{\rm x}\,n_H^{\rm x})$, and Λ_ν is a frequency-dependent cooling parameter computed using the XSPEC code of Raymond and Smith (1977). For coronal model calculations the X-ray source is placed in a thin region at the base of the wind. For shock model calculations, the differential emission measure was specified by:

$$\Gamma(r) = \begin{cases} C_1\,n_w^\alpha(r) & r \le x_0\,R_* \\ \\ C_2\,n_w^2(r) & r > x_0\,R_* \end{cases} \tag{10}$$

where n_w in the cool wind density, and C_1 and C_2 are constants constrained by the observed X-ray flux and the requirement that Γ be continuous at $r = x_0\,R_*$. If the X-ray source is uniformly distributed throughout the wind $\Gamma(r)$ would be proportional to $n_w^2(r)$. We use the formula for $r \lesssim x_o\,R_*$ to account for the finite growth time of the instabilities producing the shocks (see Owocki et al. 1988). Results are presented below for 2 values of α in Eq. (10): $\alpha = -3$, which corresponds to a very rapid increase in the X-ray emission measure near $x_o\,R_*$; and $\alpha = +1$, which leads to a less steep rise in the emission measure.

(e) UV P-Cygni Profiles

Using the ionization distributions from our wind ionization calculations, OVI P-Cygni profiles were computed using a modified version of the SEI code (Lamers et al. 1987). The code was altered so that tabulated values of $\dot{M}\,q_{\rm OVI}\,(q_{\rm OVI} \equiv$ OVI ionization fraction) could be used instead of the usual parameterized optical depth formula ((Eq. 40) of Lamers et al.). The optical depth of the blue (B) or red (R) components at the scaled wind velocity $w\,(\equiv v/v_\infty)$ is related to $\dot{M}q_{\rm OVI}$ by

$$\tau_{B,R}(w) = \dot{M}q_{OVI}(w)\cdot\frac{\pi e^2}{m_e c}\cdot\frac{A_E\,\lambda_{B,R}\,f_{B,R}}{R_*\,v_\infty^2}\,\left\{x^2\,w\,\frac{dw}{dx}\right\}^{-1} \tag{11}$$

where λ and f are the wavelength and oscillator strength of the transition, A_E is the elemental abundance, and $x \equiv r/R_*$. The "turbulent velocity" used in the line profile calculations was taken to be $0.20\,v_\infty$. This value is somewhat higher than that found by Groenewegen and Lamers (1989; $v_{\rm turb} = 0.13 \pm 0.03$) based on fits to P-Cygni profiles for CIV, NV, and SiIV resonance lines and CIII and NIV subordinate lines. It was found that the higher value of 0.20 v_∞ resulted in better agreement with the observed OVI profiles. Limb darkening effects were computed also using the parameters given by Groenewegen and Lamers.

III. Results

(a) Wind Models With No X-rays

Several calculations were performed without X-ray emission from a hot plasma source for the purpose of comparing with previously published calculations, and to assess the effects of various processes on the OVI ionization fraction. To test the fidelity of our statistical equilibrium calculations, we performed a calculation identical to the 32,500 K supergiant case reported by Drew (1989). Using atomic models and a temperature distribution reported by Drew, the spatial dependence of ionization fractions for H, He, C, N, and O were calculated and compared. For all ions except CIII the ionization distributions agreed with those reported by Drew to within a factor of 2. We consider this agreement to be quite good considering the facts that: (1) the ionization fractions often varied in the radial direction by more than an order of magnitude, and (2) identical atomic data was not used. The differences observed for CIII are simply a result of the CIII photoionization edge being very close to that of the "mean light ion" used in the Mihalas model atmosphere. It was found that a slight shift in the edge frequency could lead to very different results for the CIII fraction. This effect, which results from the use of a fictitious atom in the Mihalas calculations, demonstrates the need for accurate predictions of the radiation field in the 40 - 100 eV range. The uncertainties associated with this are likely to be the reason for the poor agreement found between theory and observation (Groenewegen and Lamers 1991) for CIII ($h\nu_1$ = 47.9 eV) and Si IV ($h\nu_1$ = 45.1 eV) ionization fractions.

To examine the influence of various physical effects on the calculated OVI fraction, we performed a series of calculations in which various parameters were adjusted. In each calculation, $\dot{M} = 4 \times 10^{-6}$ $M_\odot$/yr and X-ray emission was not included. Our base

Table 1

Calculated OV and OVI Fractions at $v = 0.5\, v_\infty$ for Wind Models With No X-rays

Ion	Case 1	Case 2	Case 3	Case 4	Case 5
OV	0.15	0.17	0.14	0.28	0.84
OVI	2.3×10^{-6}	$< 10^{-12}$	2.2×10^{-6}	2.0×10^{-5}	1.0×10^{-3}

calculation included: (1) a temperature distribution computed by Drew; (2) a relatively detailed atomic model with a total of 203 levels; (3) diffuse radiation from OIV and OV using the model described in Sec. II(d); and (4) dielectronic recombination. The OV and OVI ionization fractions for this case (Case 1) at $v = 0.5\, v_\infty$ are shown in Table 1. The bulk of the remaining oxygen is in OIV. The OVI fraction of 2×10^{-6} is seen to be much smaller than that deduced from observations ($\sim 10^{-3}$; Lamers et al. 1980). This suggests that X-rays play a dominant role in the production of OVI in the wind of ζ Pup.

The importance of properly treating ionization out of excited states can be seen in the results of Cases 1 and 2. The results for Case 2 were obtained using a relatively simple atomic model for oxygen similar to that of Drew (just 3 excited states). Virtually no OVI is predicted in this case. The OVI in Case 1 is primarily produced by photoionization out of excited states of the type $1s^2 2s^1 3l$ (l = s,p,d), which have photoionization threshholds in the range of 38 - 45 eV. These excited states tend to be populated not by direct photoexcitation from the ground state of OV, but rather by a series of excitation processes through intermediate levels.

In Case 3 diffuse radiation from OIV and OV was neglected. Comparison of results from Cases 1 and 3 indicate the OVI fractions tend to be fairly insensitive to the diffuse radiation field above the OIV edge (77.9 eV). This stems from the fact that the OVI is primarily produced by photoionization out of excited states, and therefore is sensitive to the radiation field at lower photon energies.

The above results do not confirm the conclusion reached by Pauldrach (1987), who suggested that a sufficient amount of OVI could be produced without X-ray radiation from a high temperature plasma. To attempt to understand the reasons for this discrepancy, we examined the influence of the wind temperature distribution and

dielectronic recombination on our results. Cases 4 and 5 shows results from a calculation which we assumed an isothermal wind temperature of $T = T_{\rm eff}$. In Case 4 dielectronic recombination was included, while in Case 5 it was not. It is seen that increasing the wind temperature alone results in an order of magnitude increase in the OVI fraction. It is further increased by a factor of 50 by neglecting dielectronic recombination. By comparison, Pauldrach obtained an OVI fraction of about 10^{-3} using assumptions similar to those of Case 5.

We conclude that the X-ray emission from a hot plasma source is primarily responsible for the bulk of the OVI observed in the wind of ζ Pup. If the dielectronic recombination rate coefficients calculated by Nussbaumer and Storey (1983) are even roughly correct, OVI is not likely to be produced in sufficient quantities without the presence of an X-ray source. Production of OVI without X-rays becomes even more problematic for late O and early B stars. This suggests that the OVI P-Cygni profile can be used to constrain the X-ray source characteristics. This is examined in the remainder of this section.

(b) Influence of X-rays on Oxygen and Nitrogen Ionization Distributions

We next present results which illustrate how the X-ray radiation field can affect ionization distributions of heavy element species. Figures 1 and 2 show the ionization distributions for O and N, respectively, from two calculations for ζ Pup. In the first calculation, where the results are represented by curves with open squares, no high temperature X-ray source was included in the calculation. In the second calculation, a distributed X-ray source (shock model) was included which was constrained to match the IPC and BBXRT spectral observations. The parameters for the differential emission measure in Eq. (10) were $\alpha = +1$ and $x_o = 5$. (This case is discussed in more detail in Sec. III(d).) The mass loss rate in each case was 5×10^{-6} $M_\odot$/yr.

Figures 1 and 2 show that the lower ionization stages (OIII-IV and NIII-IV) are essentially unaffected by the X-rays. This is because their photoionization rates are more sensitive to relatively low energy photons, which have large mean intensities. For high ionization stages — OVI-VII and NVI-VII — the X-rays play a dominant role in determining the ionization fractions. OV and NV represent intermediate cases where the X-rays are important at larger radii: $r \gtrsim 3R_*$ for OV and $r \gtrsim 10\,R_*$ for NV. Note that because NV is *not* predicted to be sensitive to the X-ray field in our calculations for ζ Pup, we have chosen not to attempt to use it to constrain the X-ray source characteristics.

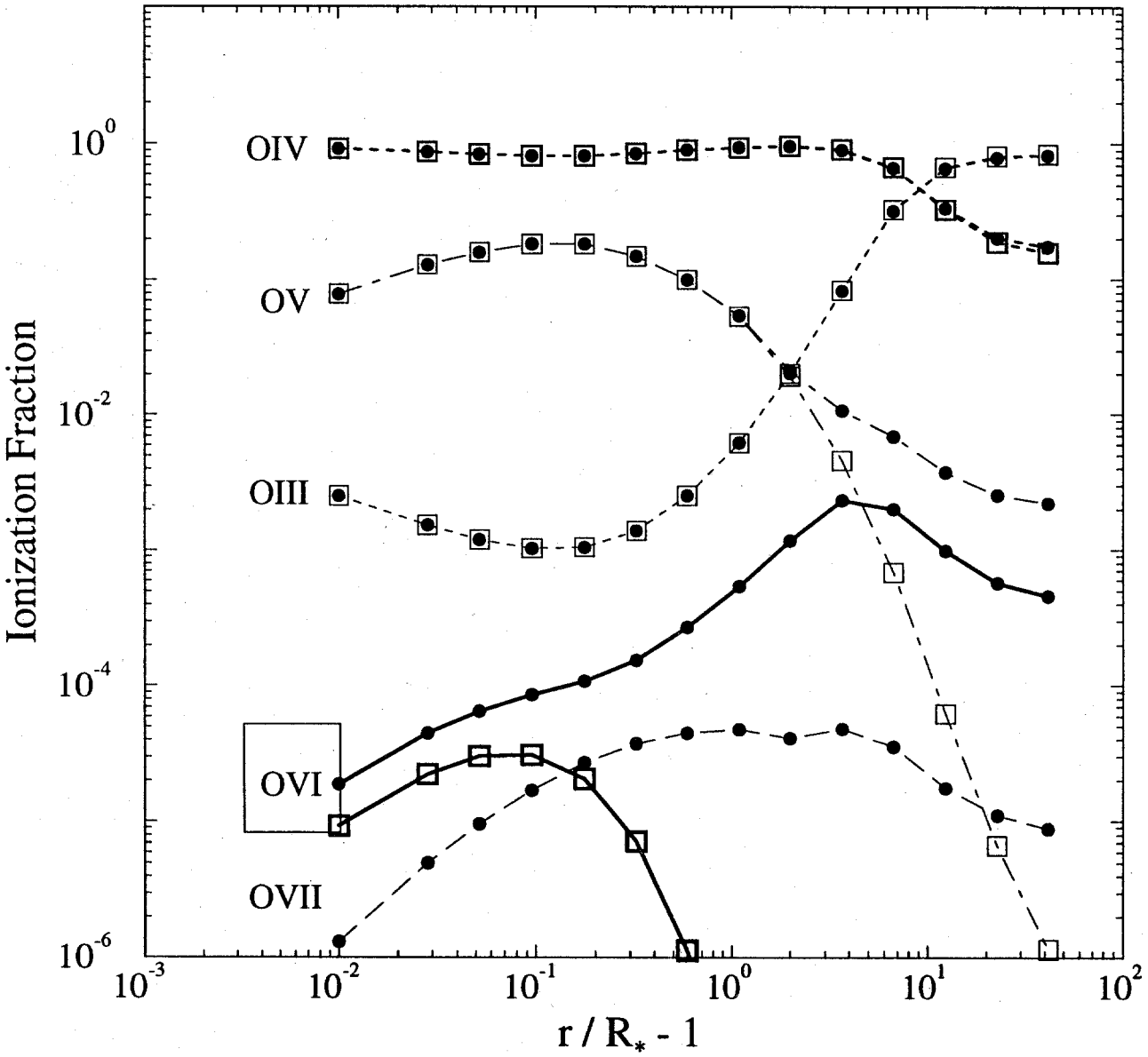

Figure 1. Ionization distributions for oxygen in the wind of ζ Pup. Curves marked with open squares (□) were calculated without an X-ray source, while those marked with filled circles (•) were computed using a distributed X-ray source (see Sec. III(d)).

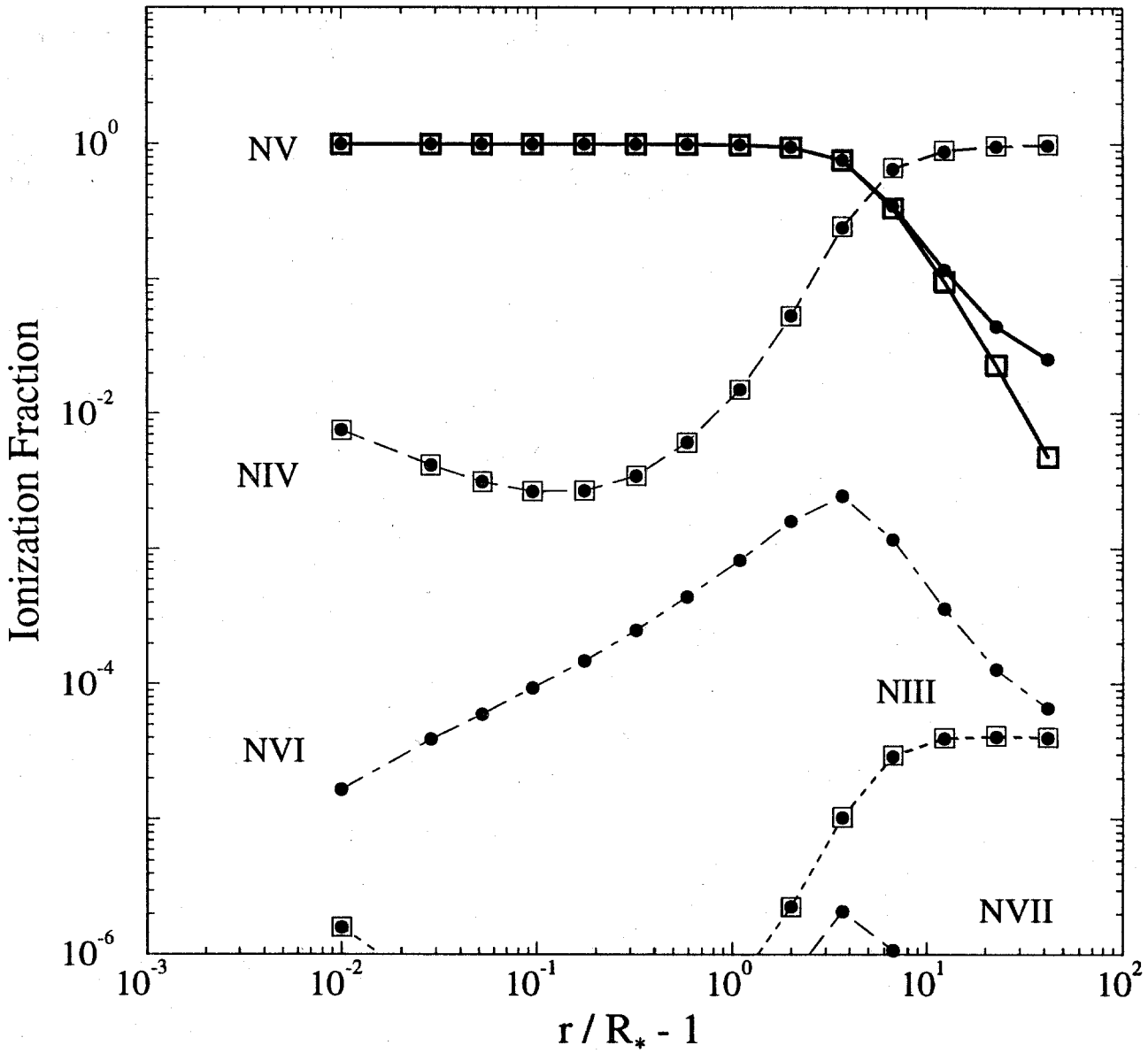

Figure 2. Same as Fig. 1, but for nitrogen.

Note that OIV is predicted to be the dominant oxygen ion out to $r \approx 10R_*$. Because of this, Auger ionization from OIV tends to be the dominant process for producing OVI. Our prediction for OIV being the dominant species is consistent with the results of Drew (1989), who provides results for OII-V at $v = 0.5\, v_\infty$ which are all in general agreement with ours. To test the sensitivity of this result to wind temperature, we performed calculations with an isothermal cool wind component of $T = 42,000$ K. We found some small differences ($\sim 10 - 20\%$) in the OIV fractions for this case as compared to results using a Drew temperature distribution.

If the OIV fraction were found to vary significantly with radius it could potentially introduce some complexities in using the OVI P-Cygni profile to deduce the location of the X-rays. However, it will be seen below that the effect that most dramatically influences the OVI profile is the reduction of X-ray intensity due to O K-shell attenuation in the cool wind. And since the K-shell opacity from OIV and OV are similar in magnitude, the primary conclusions of this paper should not be significantly affected by inaccuracies in the computed OIV distributions.

(c) Coronal Results

We next describe results from a series of coronal calculations for ζ Pup in which we examine whether the coronal hypothesis is consistent with both X-ray and UV data. In our models, the mass loss rate was varied between $\dot{M} = 1 \times 10^{-6}$ and 5×10^{-6} $M_\odot$/yr. The X-ray region consisted of a thin isothermal zone at the top of the photosphere ($R_* < r < R_{cor}$). We chose the maximum radius of the coronal region, R_{cor}, to be $1.1\, R_*$. This corresponds to a minimum cool wind velocity of $0.19\ v_\infty$. The choice of coronal radius can be important for the following reason. The optical depth at frequency ν for the overlying wind can be written as:

$$\tau_\nu \;=\; \alpha_\nu \int_{R_{cor}}^{\infty} n_w \, dr \;=\; C \int_{w(R_{cor})}^{1} dw \, w^{(\frac{1}{\beta}-2)} \,,$$

where α_ν is the absorption cross section and C is a constant. Since the cool wind component is most dense near the top of the photosphere (or corona), a significant contribution to the opacity comes from low velocity material near the base of the wind. We chose $R_{cor}/R_* = 1.1$ because it was felt that a larger value of R_{cor} would lead to a minimum velocity for the cool wind that is not consistent with observed P-Cygni profiles of the various ion species observed for ζ Pup.

For each mass loss rate, the X-ray temperature and emission measure of the coronal region were adjusted in an attempt to get a reasonable match with both the BBXRT and IPC spectral data. After this was achieved, OVI P-Cygni profiles were computed using the SEI code in conjunction with values of $\dot{M}\, q_{\rm OVI}$ predicted from the calculations. Results are shown in Figures 3 through 6 for mass loss rates of $\dot{M} = 1 \times 10^{-6}$ and 2×10^{-6} $M_\odot$/yr. OVI profiles were not calculated for higher mass loss rates because a good match with the X-ray data could not be obtained in the spectral region from 0.6 to 1.5 keV; i.e., the photon energy range just above the K-shell edge for oxygen. The X-ray temperature and emission measure for the former case was $T_{\rm x} = 5.0 \times 10^6$ K and $EM_{\rm x} = 3.0 \times 10^{56}\,{\rm cm}^{-3}$. For the latter case $T_{\rm x} = 3.2 \times 10^6$ K and $EM_{\rm x} = 2.4 \times 10^{57}\,{\rm cm}^{-3}$. Occultation by the stellar disk reduces the *observable* emission measure to about 65% of the stated values.

Figure 3 shows the calculated frequency-dependent luminosities for the $\dot{M} = 1 \times 10^{-6}$ (top) and 2×10^{-6} $M_\odot$/yr (bottom) cases. In each case the carbon K-edge near 0.39 keV and oxygen K-edge near 0.64 keV are clearly present. The "spikes" in the spectra are line emission from the hot plasma region as predicted by XSPEC. The exception to this is at $h\nu = 0.11$ keV, which is due to the diffuse radiation field which is dominated by the recombination of OVI to OV. Since this results from the approximation used in Eq. (8) to describe the diffuse radiation field, it is not clear whether this feature provides an accurate representation of this portion of the spectral region.

The optical depths for the two cases are shown in Figure 4. Longward of the HeII edge (54 eV), the continuum optical depth is very small ($< 10^{-2}$). Just shortward of the HeII edge the optical depth rises to about 10 and 30 for the low and high mass loss rates respectively. Most of this opacity arises from material at large radii ($r \gtrsim 10\,R_*$) because the HeII fraction increases with radius. The OIV and OV edges arising from ground state to ground state transitions are prominent at 77 and 114 eV, respectively, as is the edge at 88 eV arising from the $1s^2 2s^2 2p^1\ ^2P$ to $1s^2 2s^1 2p^1\ ^3P$ transition. The carbon and oxygen K-edges in the $\dot{M} = 2 \times 10^{-6}$ $M_\odot$/yr case have peak optical depths of about 5 and 8, respectively. The nitrogen edges are not very prominent because its assumed abundance is low (O/N $\approx$ 7.2 and C/N $\approx$ 3.6).

To compare with observational data, the computed fluxes were fed through instrumental response programs for BBXRT and IPC. Comparison of the model predictions and observations are shown in Figure 5. The top plot shows the BBXRT results while the lower plot shows the IPC results. In each case the $\dot{M} = 1 \times 10^{-6}$ and

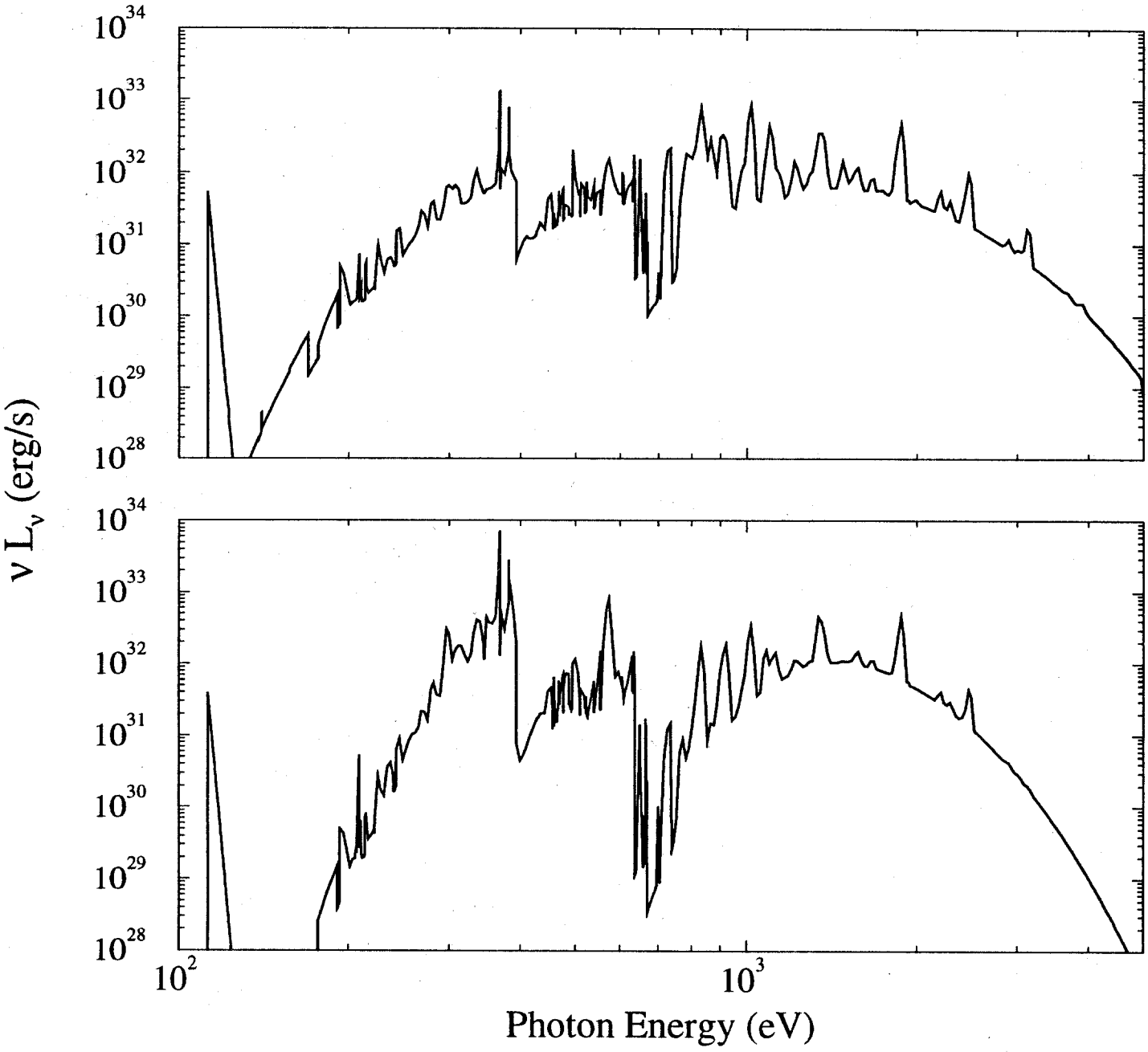

Figure 3. Calculated frequency-dependent luminosity for coronal model calculations with $\dot{M} = 1 \times 10^{-6}$ (top) and 2×10^{-6} (bottom) $M_\odot$/yr.

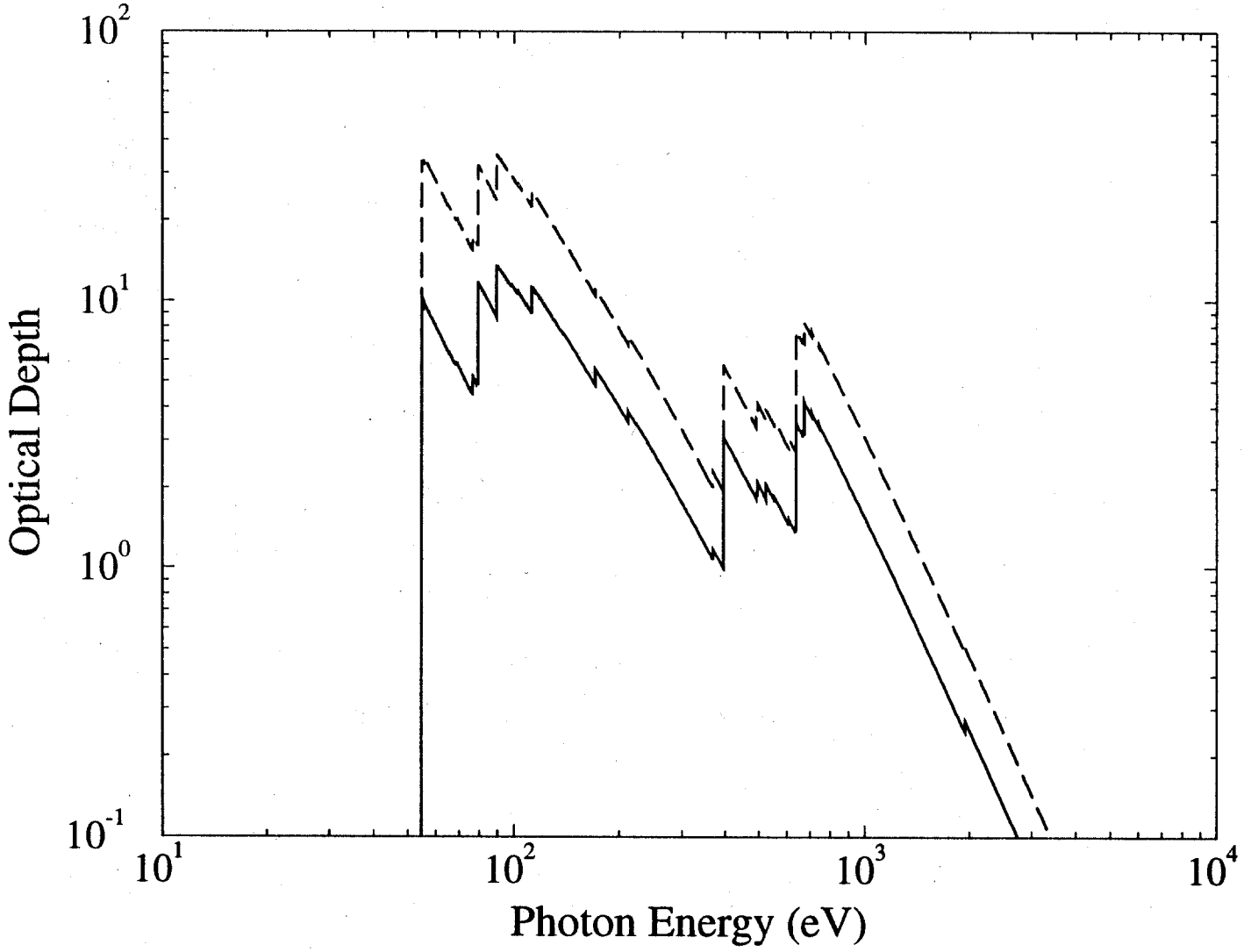

Figure 4. Frequency-dependent wind optical depths for coronal models with $\dot{M} = 1 \times 10^{-6}$ (solid curve) and 2×10^{-6} $M_\odot$/yr (dashed curve), calculated in radial direction from top of corona to infinity.

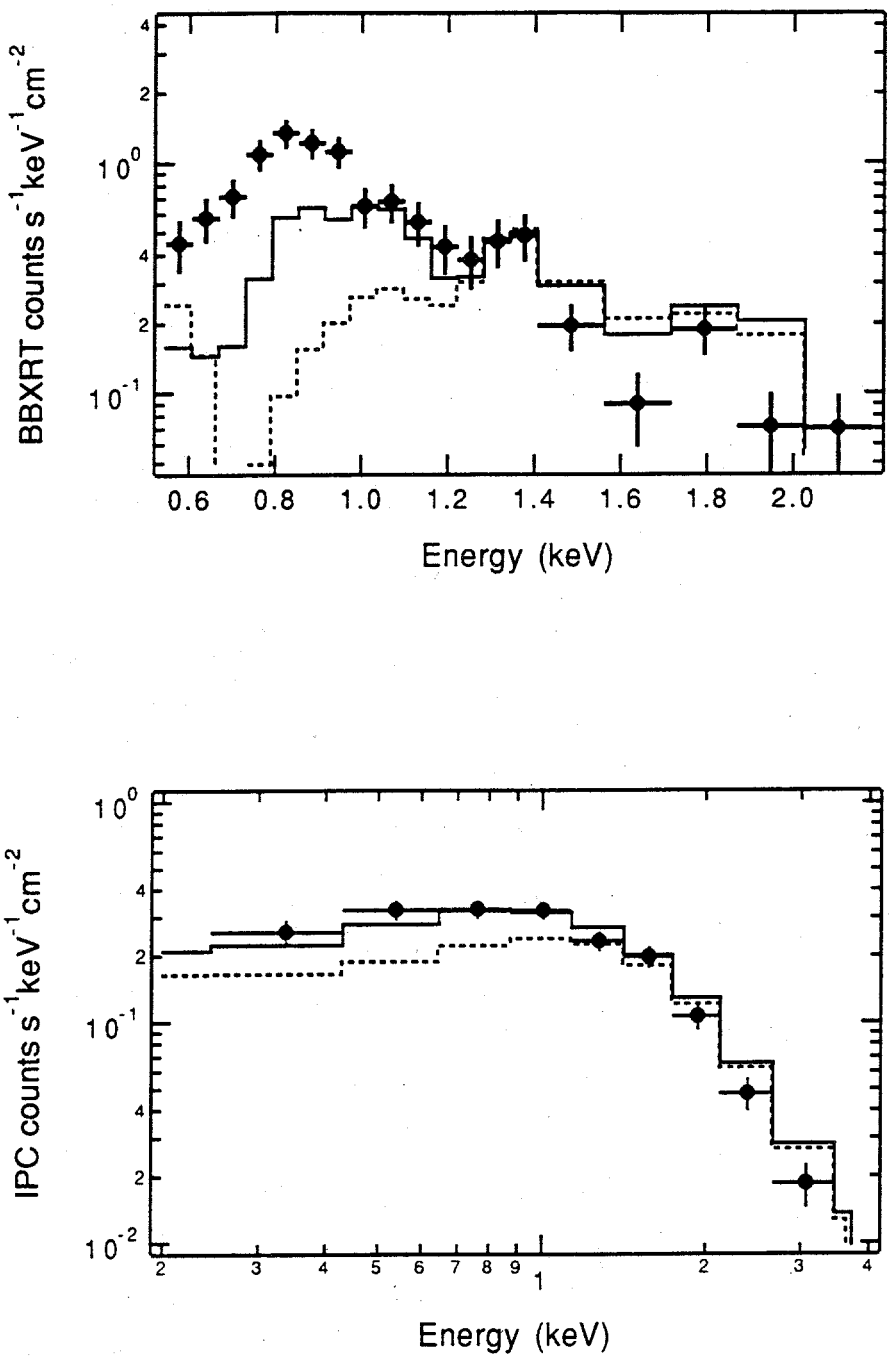

Figure 5. Comparison of BBXRT (top) and *Einstein* IPC (bottom) spectral data with coronal model results for $\dot{M} = 1 \times 10^{-6}$ (solid curve) and 2×10^{-6} $M_\odot$/yr (dashed curve).

2×10^{-6} $M_\odot$/yr cases are represented by solid and dashed curves, respectively. Note that the BBXRT spectral range is smaller than IPC, but the spectral resolution is substantially better. In fact, the feature near 1.3 keV has been attributed to Mg XI line emission, which is indicative of a plasma temperature of about $6 - 8 \times 10^6$ K (Corcoran et al. 1992).

For the $\dot{M} = 1 \times 10^{-6}$ $M_\odot$/yr case, the model predictions are in reasonable agreement with both the BBXRT and IPC data. The calculated spectrum is typically within about a factor of 2 of the data, although deviations from the BBXRT data are somewhat larger below 0.8 keV. A softer spectrum using a lower X-ray temperature might produce somewhat better agreement with the BBXRT data, but the IPC agreement would be worse. It is worth noting, however, that the BBXRT and IPC observations were made at different times (several years apart), and that the X-rays from ζ Pup are known to vary with time (Collura et al. 1989). Thus, the X-ray source characteristics may have been somewhat different at the times of the BBXRT and IPC observations.

The optical depth at the K-shell edge in the lower mass loss calculation is about 4, which is marginally consistent with the analysis of Corcoran et al., who found $1.0 < \tau < 3.6$. Given the assumptions in the model (isothermal temperature for the X-ray source, cosmic abundances), we consider the agreement with the X-ray data for this model to be satisfactory. Clearly, a better fit to the data could be obtained by using a multi-temperature model or by adjusting the elemental abundances.

For higher mass loss rates the agreement between the calculated fluxes and observation deteriorates rapidly. In the IPC plot, the calculated fluxes from 0.4 to 1.0 keV for the $\dot{M} = 2 \times 10^{-6}$ $M_\odot$/yr case are somewhat depressed relative to the data because of C and O K-shell absorption. The overall agreement, however, is not particularly bad. The discrepancies with the BBXRT data are much more pronounced. Oxygen absorption results in a calculated flux which is a factor of 3 to 10 too low in the 0.7 to 1.0 keV range. It is also worth noting the Mg XI line emission detected by BBXRT at 1.3 keV (Corcoran et al. 1992) decreases for a lower temperature X-ray source (Raymond and Smith 1977). Because of BBXRT's higher spectral resolution, the constraints on X-ray source models are much more stringent.

The above results suggest that the coronal hypothesis could be valid for ζ Pup only if $\dot{M} \lesssim 1 \times 10^{-6}$ $M_\odot$/yr. This represents a value which is a factor 3.5 and 5.0 lower than that suggested by the radio data of Abbott et al. (1980) and Bieging et al. (1989). Although this poses a serious problem for the coronal hypothesis, it does not rule out

the possibility that there could be significant X-ray emission from a corona at the wind base for several reasons. Firstly, the radio data in some sense should represent an upper limit to the mass loss rate. Any "clumping" in the wind due to density enhancements or a non-spherical mass distribution could lead to an overestimate of the mass loss rates deduced from radio data, as discussed by Abbott et al. (1981). In addition, magnetic fields in the wind can enhance radio flux and lead to overestimates of mass loss rates (Maheswaran and Cassinelli 1992). Secondly, the primary discrepancy with the X-ray data arises from oxygen absorption. If oxygen is significantly depleted in the atmosphere of ζ Pup relative to the cosmic value, the attenuation is of course reduced. Any depletion of heavy elements would have relatively little effect on the radio data interpretation. We know of no studies, however, which support such a depletion. Thirdly, it is also possible that the X-rays could be emitted by both shocked material embedded in the wind and a corona at the base, with the corona emitting relatively hard X-rays which are not as affected by cool wind attenuation. But if the mass loss rate deduced from radio observations is approximately correct and there is no significant oxygen depletion, the constraints imposed in particular by the BBXRT data strongly suggest that at least the soft component of the X-rays comes from a source that is embedded in the wind.

If the mass loss rate is in fact lower than the values determined from radio observations, one might ask whether the OVI P-Cygni profiles are consistent with a base corona. Figure 6 shows the P-Cygni profiles computed using the values of $\dot{M} q_{\rm OVI}(r)$ from the $\dot{M} = 1 \times 10^{-6}$ and 2×10^{-6} $M_\odot$/yr cases. The results are compared with the observed profile extracted from Morton (1976). The emission peaks from the model calculations are seen to be somewhat high relative to the data. But since the overall agreement is reasonable, we cannot rule out these models from the UV data alone. We conclude that the coronal hypothesis for ζ Pup is consistent with both UV and X-ray observations if $\dot{M} \lesssim 1 \times 10^{-6}$ $M_\odot$/yr. And since the X-ray emission measure is $< 10^{57}$ cm^{-3}, such a model is not inconsistent with the observations of Baade and Lucy (1987).

(d) Distributed X-ray Emission (Shock) Calculations

If X-rays are emitted from a region above the base of the wind, is it possible to place some constraints on the source location from the OVI profile? Numerical simulations by Owocki (1991) and Owocki et al. (1988) suggest that strong shocks can begin forming due to radiative driven instabilities by $r \approx 1.3\, R_*$. On the other hand, Chlebowski (1989) suggests the X-rays may originate at a point far from the star due to the interaction of

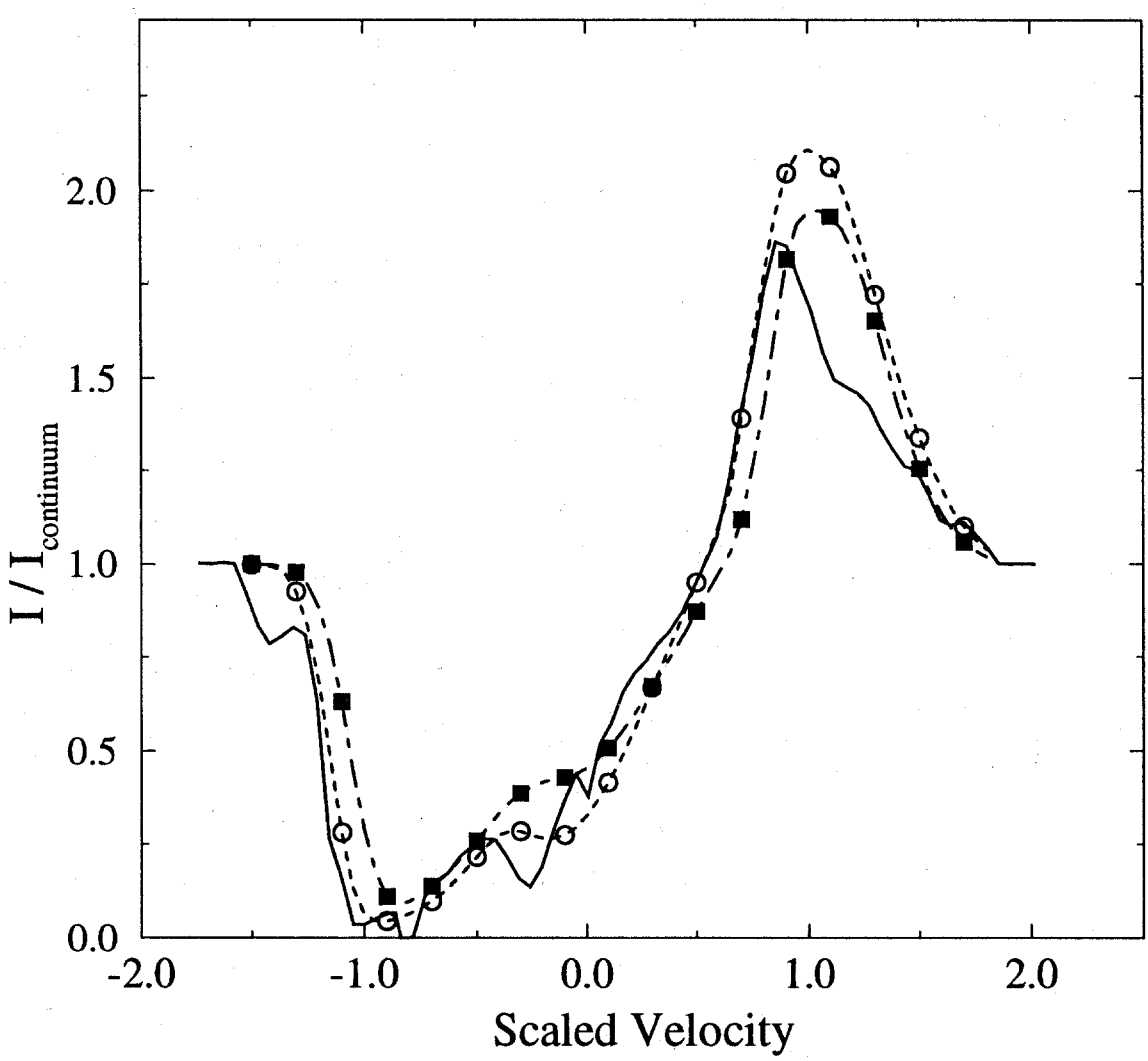

Figure 6. Comparison of observed OVI P-Cygni profile for ζ Pup (solid curve) with calculated profiles for coronal models with $\dot{M} = 1 \times 10^{-6}$ (curve with open circles) and 2×10^{-6} $M_\odot$/yr (curve with filled squares).

the wind with circumstellar matter. To address the question of X-ray source location, we performed a series of calculations in which the distribution of the X-ray emission from the wind was varied.

In the first series of calculations the X-ray emission measure distribution was specified using Eqs. (9) and (10) with $\alpha = -3$. The value of x_o was varied from 1.3 to 4.0. In these models, there is little X-ray emission emitted from regions of the wind where $r/R_* < x_o$. This is shown in Figure 7, where the cumulative emission measure for each of the 3 calculations in this series is plotted as a function of scaled velocity ($= v/v_\infty$). The total X-ray emission measure and temperature were adjusted to produce reasonably good agreement with the BBXRT and IPC data. The total emission measure increases as x_o decreases because of the greater attenuation by the overlying wind. In each case the X-ray temperature was $10^{6.8}$ K (6.3×10^6 K) and the mass loss rate was 5×10^{-6} $M_\odot$/yr.

The resulting spectra are compared with BBXRT and IPC observations in Figure 8. In each case the agreement between the calculated spectrum and observation is reasonably good, although the calculated fluxes are somewhat low below 0.7 and near 1.3 keV. As x_o decreases the spectrum is slightly softer because of increased attenuation. It does not, however, become drastically softer because much of the emission comes from $r/R_* > x_o$. Corcoran et al. (1992) found that better fits to the BBXRT spectrum could be obtained by lowering the Fe abundance (which lowers the emission in the 0.8 – 1.1 keV range) and increasing the Mg abundance (which produces a higher peak at 1.3 keV). One could alternatively attempt to use multi-temperature models to produce a better fit with the data. In the present paper we have chosen not to do this because our primary goal is to investigate the dependence of the OVI P-Cygni profile on X-ray source properties. It is therefore felt the agreement between the calculated spectra and observations is quite adequate.

The OVI ionization distributions for each case are shown in Figure 9 as a function of scaled velocity. In each case the ionization fraction peaks at a radius of $r \approx x_o\, R_*$ with $\dot{M} q_{\rm OVI} \approx 1.0{-}1.5{\times}10^{-8}$ (or $q \approx 2{-}3{\times}10^{-3}$). Below this, the ionization fraction decreases rapidly as the photosphere is approached. This occurs because X-rays originating from points far above the photosphere cannot penetrate through the intervening cool wind to Auger ionize material at lower levels. This attenuation by material between $r = R_*$ and, say, $r = 2\, R_*$ is exactly the same phenomenon which causes serious problems for coronal models. At lower velocities ($v \lesssim 0.3\, v_\infty$) an increase in the OVI fraction is caused by non-Auger processes (see Figure 1).

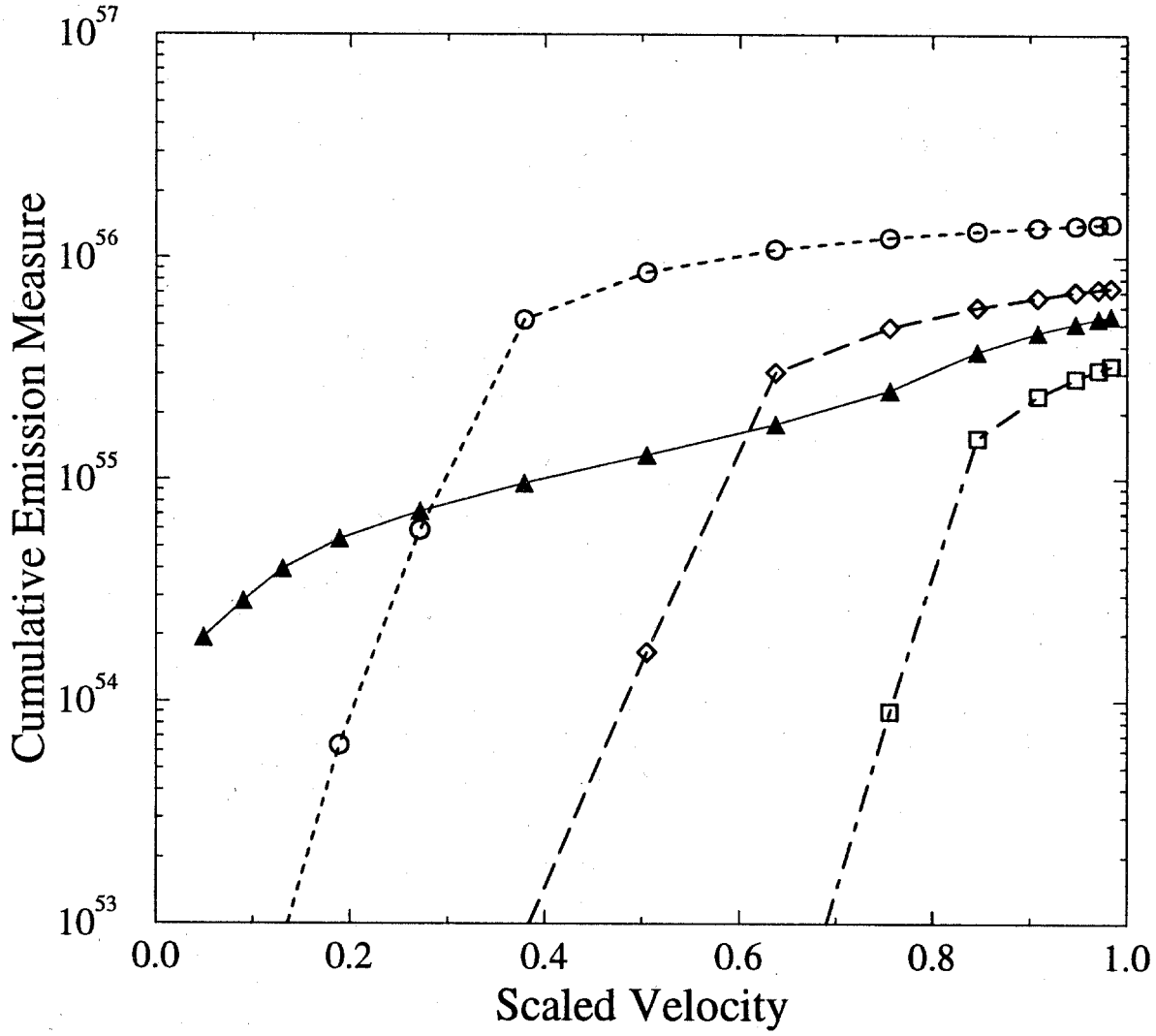

Figure 7. X-ray emission measure distributions used in shock model calculations plotted as a function of scaled velocity ($= v/v_\infty$). The curves with open symbols correspond to cases with $\alpha = -3$ and $x_o = 1.3$ (circles), $x_o = 2.0$ (diamonds), and $x_o = 4.0$ (squares). The curve with filled triangles corresponds to the case with $\alpha = +1$ and $x_o = 5.0$. The parameters α and x_o are defined in Eq. (10).

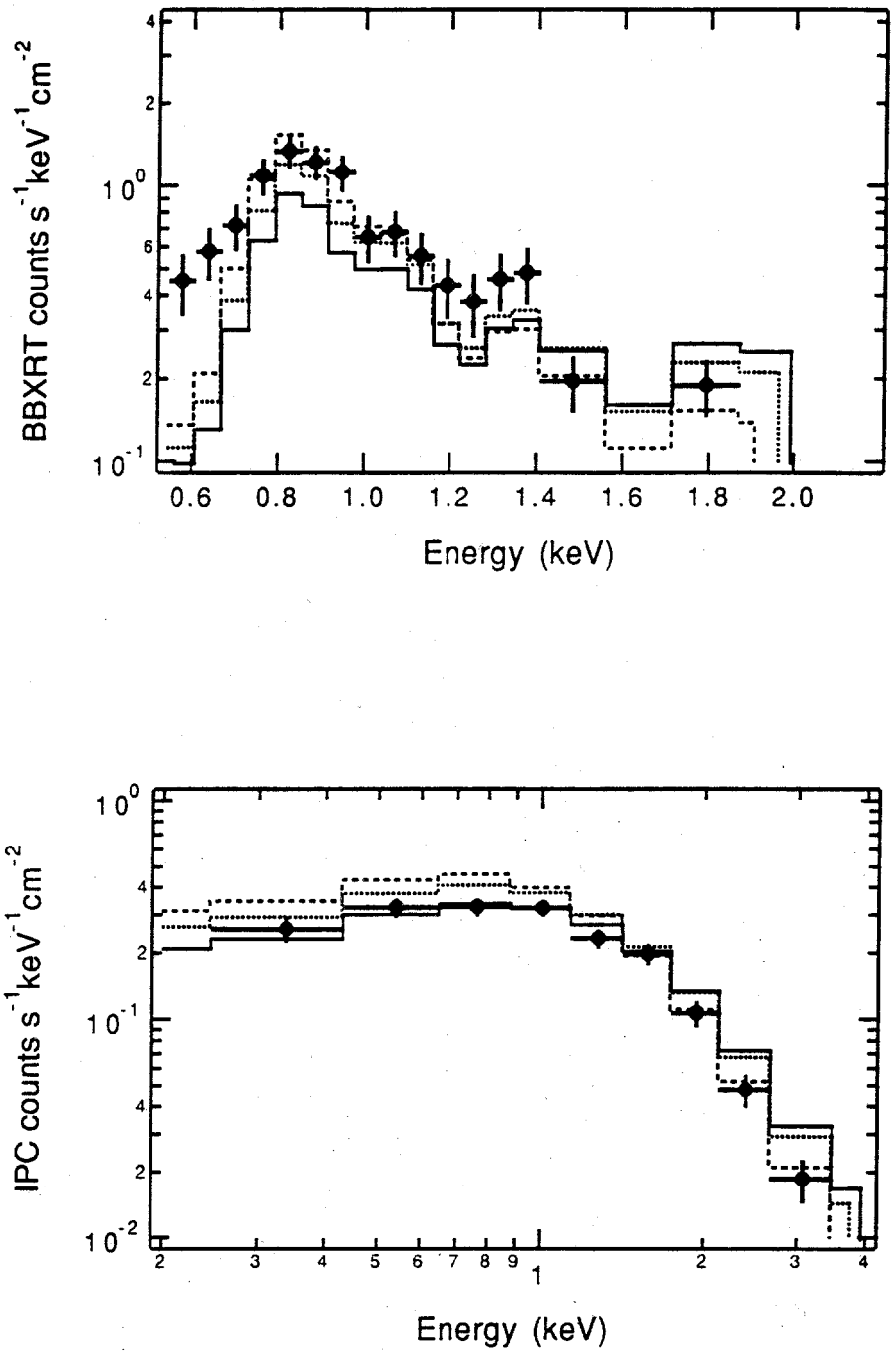

Figure 8. Comparison of observed X-ray spectra for ζ Pup (error bars) and calculated spectra from distributed X-ray emission models with $\alpha = -3$, and $x_o = 1.3$ (solid curve), $x_o = 2.0$ (dotted curve), and $x_o = 4.0$ (dashed curve).

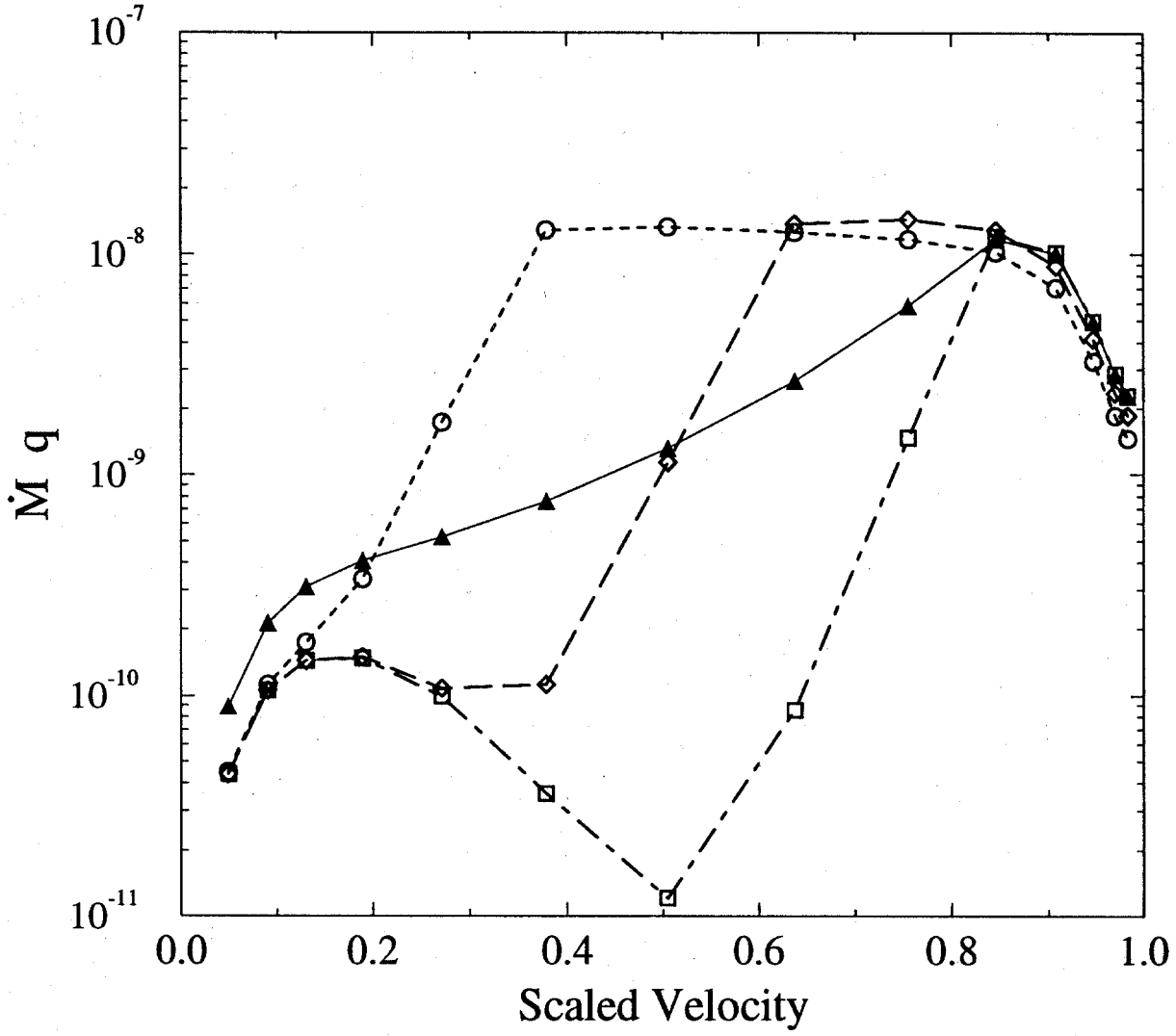

Figure 9. Product of mass loss rate times OVI ionization fraction as a function of scaled velocity for distributed X-ray emission models. The curves with open symbols correspond to cases with $\alpha = -3$ and $x_o = 1.3$ (circles), $x_o = 2.0$ (diamonds), and $x_o = 4.0$ (squares). The curve with filled triangles corresponds to the case with $\alpha = +1$ and $x_o = 5.0$. The parameters α and x_o are defined in Eq. (10).

For the $x_o = 4$ case it is seen that the OVI fraction remains very low until $v \approx 0.8\, v_\infty$. That is, if very few X-rays originate below $4R_*$, one should expect relatively little OVI to exist in the region of the wind where velocities are low and densities are high. As more and more X-rays are generated at smaller radii (see $x_o = 1.3$ and 2.0 cases), more OVI is produced in the low velocity material.

The effect of the OVI distribution on its P-Cygni profile is shown in Figure 10. For the $x_o = 1.3$ case the general shape of the profile is similar to the observed profile. The emission peak is a little too high and the absorption at $w \approx 0$ is somewhat strong, indicating the OVI fraction is slightly high. Nevertheless, the overall qualitative agreement with observation is quite reasonable. At the other extreme, the $x_o = 4$ case shows very little in the way of an emission peak. The profile for this case shows 2 distinct absorption features due to the red and blue components. The absence of a pronounced emission peak is due to the fact that there is little OVI in the high density portion of the wind. Even for the $x_o = 2$ case the emission feature begins to become less peaked. Thus, our results strongly suggest that there is a significant source of X-ray emission located within $2\, R_*$.

Somewhat better agreement with the observed profile is attained when the X-ray emission is distributed more uniformly throughout the wind. Figure 11 shows the profile computed for the case of $\alpha = +1$ and $x_o = 5$. The corresponding distributions of emission measure and $\dot{M} q_{\rm OVI}$ are represented by the curves with triangles in Figures 7 and 9. In this case the OVI fraction rises more slowly with velocity out to $r \approx 5\, R_*$. The peak is reduced relative to the $x_o = 1.3$ case in Figure 10, and is in better agreement with the observed peak. In this particular case, roughly one-third of the total emission measure originates from $r < 2\, R_* (v < 0.6\, v_\infty)$. The results again show that there must be a substantial X-ray flux originating from material at $r \lesssim 2\, R_*$.

These results are consistent with the theory that strong shocks form rapidly in the lower regions of the wind where the radiative driving force is large (Owocki et al. 1988). Although shocked X-ray emitting regions may also exist at larger radii, their X-rays should have little effect on the OVI production at low velocities. Our results present very serious problems for any hypothesis which suggests that all X-rays originate from regions far above the photosphere (more than a few R_*). Thus, the Chlebowski (1989) suggestion that the X-rays may be due to the interaction of the wind with circumstellar matter is *not* consistent with our results.

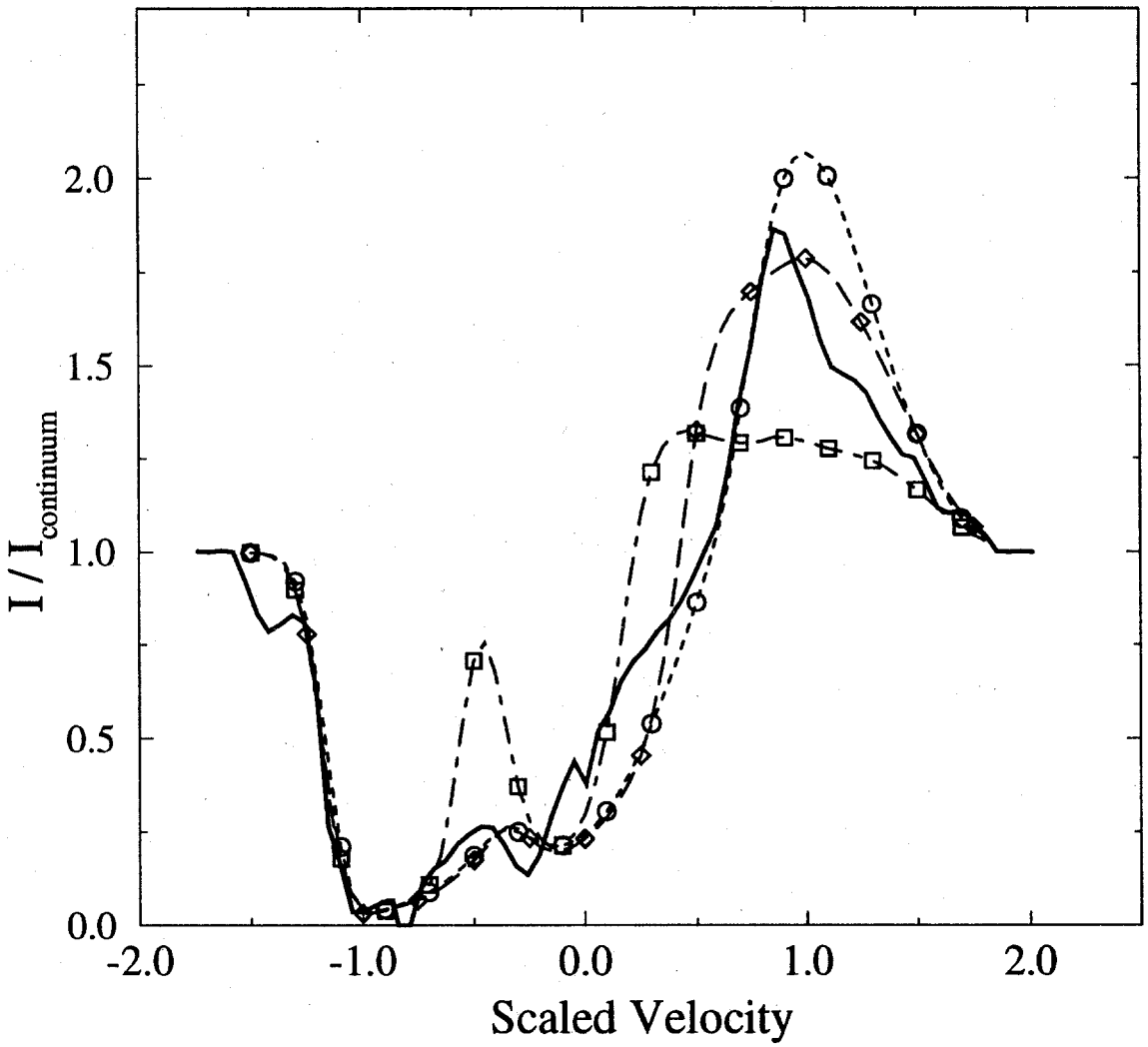

Figure 10. Comparison of observed OVI P-Cygni for ζ Pup (solid curve) with those computed from distributed X-ray emission models with $\alpha = -3$, and $x_o = 1.3$ (dotted curve with circles), $x_o = 2.0$ (dashed curve with diamonds), and $x_o = 4.0$ (dash-dotted curve with squares.)

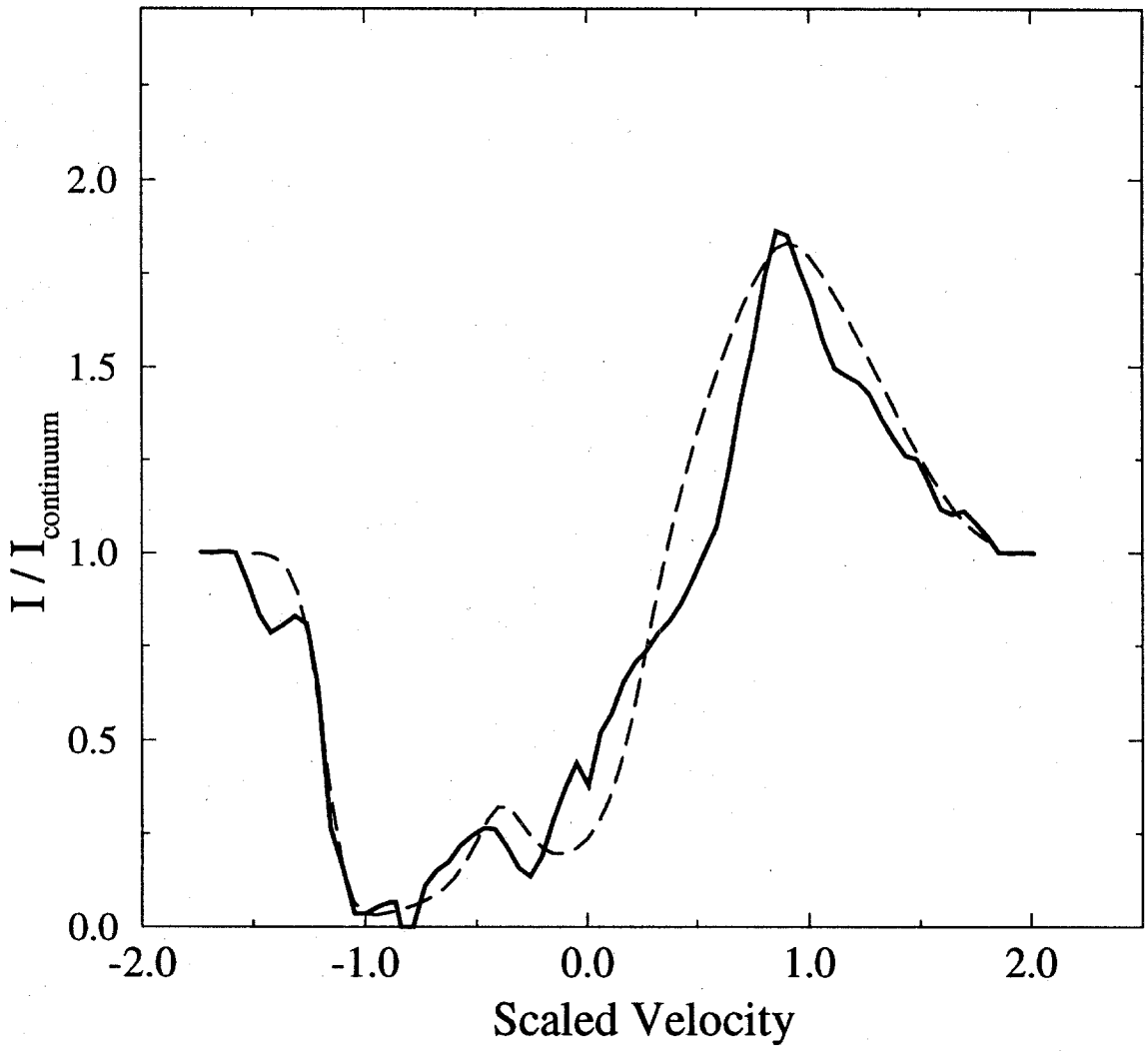

Figure 11. Same as Fig. 10, but for the distributed X-ray emission case with $\alpha = 1$ and $x_o = 5$. The observed and calculated profiles are represented by the solid and dashed curves, respectively.

IV. Summary

We have presented results from detailed wind ionization calculations which show how the OVI ionization fraction and its P-Cygni profile are affected by X-ray source characteristics. Detailed atomic models were used in an attempt to simulate as accurately as possible the complex array of radiative and collisional processes that can occur in hot star winds. Calculations were performed with and without a hot plasma X-ray source to examine whether sufficient amounts of OVI can be produced without X-rays. Our results indicate the OVI in the wind of ζ Pup is produced primarily by X-ray photoionization. This contradicts the conclusion by Pauldrach (1987). Because of its dependence on the X-ray flux, we find that OVI P-Cygni profiles provide useful constraints for investigating the characteristics of hot star X-ray sources.

Our results also indicate that a significant X-ray flux originates from regions within 2 stellar radii. This is due to the fact that the soft X-rays that produce OVI are strongly attenuated by cool wind material in this region. X-rays originating at radii more than a few stellar radii cannot be transported downward to produce sufficient amounts of OVI in the high density, low velocity region. In the absence of a substantial source of X-rays at $r \lesssim 2\,R_*$, calculated OVI P-Cygni profiles were shown to have reduced emission peaks and were not in agreement with the observed profile for ζ Pup. Our results are therefore not compatible with the suggestion by Chlebowski (1989) that X-rays originate far from the star.

We find that an exclusively coronal source for ζ Pup is consistent with both X-ray and UV observations only if either $\dot{M} \lesssim 1 \times 10^{-6}$ $M_\odot$/yr, or there is a significant depletion of oxygen in its upper atmosphere. This mass loss rate is a factor of 3.5 and 5.0 lower than the radio-deduced values of Abbott et al. (1980) and Bieging et al. (1989), respectively. The coronal models described in this paper have significantly lower X-ray emission measures and mass loss rates than those described by Cassinelli et al. (1981) and Waldron (1984). The restriction for low mass loss rates results in large part from the more stringent constraints imposed by recent higher-resolution BBXRT observations (Corcoran et al. 1992). Because of the lower coronal emission measures, the optical observations of Baade and Lucy (1987) do not rule out the possibility of a coronal X-ray source. Nevertheless, the discrepancies that arise between X-ray and radio observations still pose serious problems for the coronal hypothesis.

We have presented results from distributed X-ray emission calculations which are simultaneously consistent with X-ray, radio, and OVI UV observations. Using a mass loss rate consistent with radio data, our results suggest that strong shocks likely begin forming at $r \lesssim 2\,R_*$. These results are consistent with radiation-hydrodynamics simulations of Owocki (1991) and Owocki et al. (1988), who predict strong shocks start to form due to line driven instabilities at $r \approx 1.3\,R_*$. Thus, if the radio-deduced mass loss rate is approximately correct, the argument that radiatively-driven instabilities lead to the rapid formation of wind shocks is supported not only by X-ray observations, but also by the OVI P-Cygni profile of ζ Pup.

Acknowledgements

The authors thank H.J.G.L.M. Lamers for supplying a recent version of his SEI code. J.J. MacFarlane and J.P. Cassinelli are supported in part by NASA Grant NAGW-2210. M.F. Corcoran is supported in part by a National Research Council Resident Research Associateship at the Goddard Space Flight Center, Greenbelt, MD. M.J. Wolff is supported by a NASA Graduate Student Research Program fellowship.

References

Abbott, D.C., Bieging, J.H., Churchwell, E., and Cassinelli, J.P. 1980, *Ap. J.*, **238**, 196.

Abbott, D.C., Bieging, J.H., and Churchwell, E. 1981, *Ap. J.*, **250**, 645.

Allen, C.W. 1973, Astrophysical Quantities, Third Edition (London, Athlone).

Baade, D., and Lucy, L.B. 1987, *Astron. Astrophys.*, **178**, 213.

Bieging, J.H., Abbott, D.C., and Churchwell, E. 1989, *Ap. J.*, **340**, 518.

Burgess, A., and Summer, H.P. 1976, *M.N.R.A.S.*, **174**, 345.

Cassinelli, J.P., and Olson, G.L. 1979, *Ap. J.*, **229**, 304.

Cassinelli, J.P., and Swank, J.H. 1983, *Ap. J.*, **271**, 681.

Cassinelli, J.P., Waldron, W.L., Sanders, W.T., Harnden, F.R., Rosner, R., and Vaiana, G.S. 1981, *Ap. J.*, **250**, 677.

Castor, J.I. 1970, *M.N.R.A.S.*, **149**, 111.

Chen, W., and White, R.L. 1991, *Ap. J.*, **366**, 512.

Chlebowski, T. 1989, *Ap. J.*, **342**, 1091.

Chlebowski, T., Harnden, F.R., and Sciortino, S. 1989, *Ap. J.*, **341**, 427.

Collura, A., Sciortino, S., Serio, S., Vaiana, G.S., Harnden, F.R., and Rosner, R. 1989, *Ap. J.*, **338**, 296.

Corcoran, M.F., Swank, J.H., Serlemitsos, P.J., Boldt, E., Petre, R.P., Marshall, F.E., Jahoda, K., Mushotzky, R., Szymkowiak, A., Arnaud, K., Smale, A.P., Weaver, K., and Holt, S.S. 1992, *Ap. J.*, in press.

Drew, J. 1989, *Ap. J. Suppl.*, **71**, 267.

Groenewegen, M.A.T., and Lamers, H.J.G.L.M. 1989, *Astron. Astrophys. Suppl. Ser.*, **79**, 359.

Groenewegen, M.A.T., and Lamers, H.J.G.L.M. 1991, *Astron. Astrophys.*, **243**, 429.

Klein, R.I., and Castor, J.I. 1978, *Ap. J.*, **220**, 902.

Harnden, F.R., Branduardi, G., Elvis, M., Gorenstein, P., Grindlay, J., Pye, J.P., Rosner, R., Topka, K., and Vaiana, G.S. 1979, *Ap. J.*, **234**, L51.

Lamers, H.J.G.L.M., Cerruti-Sola, M., and Perinotto, M. 1987, *Ap. J.*, **314**, 726.

Lamers, H.J.G.L.M., and Morton, D.C. 1976, *Ap. J. Suppl.*, **34**, 715.

Lamers, H.J.G.L.M., Gathier, R., and Snow, T.P. 1982, *Ap. J.*, **258**, 186.

Lamers, H.J.G.L.M., Gathier, R., and Snow, T.P. 1980, *Ap. J. (Letters)*, **242**, L33.

Long, K.S., and White, R.L. 1980, *Ap. J.*, **239**, L65.

Lucy, L.B., and White, R.L. 1980, *Ap. J. (Letters)*, **239**, L65.

Lucy, L.B. 1982, *Ap. J.*, **255**, 286.

MacFarlane, J.J., and Cassinelli, J.P. 1989, *Ap. J.*, **347**, 1090.

Maheswaran, M., and Cassinelli, J.P. 1992, *Ap. J.*, **386**, 695.

Mihalas, D. 1972, *NCAR Tech. Note*, STR-76.

Mihalas, D. 1978, Stellar Atmospheres, Second Edition (Freeman, New York).

Morton, D.C. 1976, *Ap. J.*, **203**, 386.

Mullen, D.J. 1984, *Ap. J.*, **283**, 303.

Nussbaumer, H., and Storey, P.J. 1983, *Astron. Astrophys.*, **126**, 75.

Nussbaumer, H., and Storey, P.J. 1984, *Astron. Astrophys. Suppl. Ser.*, **56**, 293.

Olson, G.L. 1978, *Ap. J.*, **266**, 124.

Olson, G.L., and Castor, J.I. 1981, *Ap. J.*, **244**, 179.

Owocki, S.P., and Rybicki, G.B. 1984, *Ap. J.*, **284**, 337.

Owocki, S.P., Castor, J.I., and Rybicki, G.B. 1988, *Ap. J.*, **235**, 914.

Owocki, S.P., and Rybicki, G.B. 1986, *Ap. J.*, **309**, 127.

Owocki, S.P. 1991, in Stellar Atmospheres: Beyond Classical Models, eds. I. Hubeny and L. Crivellari, NATO Advanced Study Workshop (Khiwer: Dordrecht).

Pauldrach, A. 1987, *Astron. Astrophys.*, **183**, 295.

Raymond, and Smith 1977, *Ap. J. Suppl. Ser.*, **35**, 419.

Sciortino, S., Vaiana, G.S., Harnden, F.R., Ramella, M., Morossi, C., Rosner, R., and Schmitt, J.H.H.M. 1990, *Ap. J.*, **361**, 621.

Seward, F.D., Forman, W.R., Giacconi, R., Griffith, R.C., Harnden, F.R., Jones, C., and Pye, J.P. 1979, *Ap. J. (Letters)*, **234**, L55.

Sobelman, I.I., Vainshtein, L.A., and Yukov, E.A. 1981, Excitation of Atoms and Broadening of Spectral Lines (Springer-Verlag, New York).

Waldron, W.L. 1984, *Ap. J.*, **282**, 256.

Wang, P. 1991, Ph.D. Dissertation, Dept. of Nuclear Engineering and Engineering Physics, University of Wisconsin, Madison, WI.